SPACE SCIENCES

Origin of reconnecting current sheets in shocked turbulent plasma

Shimou Wang[1,2,3]†, San Lu[1,2,3]†, Quanming Lu[1,2,3]*, Rongsheng Wang[1,2,3]*, Junyi Ren[1,2,3], Xinliang Gao[1,2,3], Jin Guo[1,2,3]

Magnetic reconnection, the rearrangement of magnetic field topologies, is a fundamental plasma process throughout the universe, which converts magnetic energy to plasma kinetic energy and results in particle energization. A current sheet is a prerequisite for the occurrence of magnetic reconnection. It has been well documented that reconnecting current sheets are prevalent in turbulent plasmas. However, how these current sheets are formed remains unclear. Among natural plasmas, the region downstream of the Earth's bow shock, the magnetosheath, is one of the most turbulent. Here, we show that the reconnecting current sheets in the turbulent magnetosheath originate from the waves in the region upstream of the shock. Once excited, the upstream waves are transmitted across the shock, compressed, and then transformed into current sheets in the downstream region. Magnetic reconnection subsequently occurs in these downstream current sheets. This process can be generalized to various shocked plasmas in astrophysical and laboratorial environments where turbulent magnetic reconnection should be common.

INTRODUCTION

The high-speed solar wind slows down after it passes the Earth's bow shock, forming the magnetosheath, the downstream region of the bow shock. The plasma in the magnetosheath is intrinsically turbulent, with highly fluctuating plasma flows and electromagnetic fields (*1*–*3*). The highly fluctuating magnetic fields in the turbulent magnetosheath correspond to strong, filamentary current sheets, and magnetic reconnection (*4*) occurs in these current sheets, which dissipates magnetic energy into plasma kinetic energy by rearranging the topologies of the magnetic fields in the current sheets (*5*–*15*). The magnetic reconnection in these current sheets can form various coherent structures, e.g., flux ropes, which render the magnetosheath more turbulent, expediting the energy dissipation and particle energization therein (*16*, *17*). How are these downstream current sheets formed? To answer this question, we need to backtrace to the upstream region of the bow shock. The upstream region is particularly active when the magnetic field therein is mostly parallel to the shock normal, and a foreshock region is formed, which is filled with plenty of waves (*18*–*20*). Recent simulations have suggested that after being excited, the foreshock waves are then convected toward the shock by the high-speed solar wind, and they are eventually transmitted through the shock, during which the waves are compressed and transformed into current sheets in the downstream region where magnetic reconnection can occur (*21*–*24*). However, evidence of such a process is lacking. Here, we report spacecraft in situ detection of the evolution of plasma waves across the quasi-parallel bow shock from the foreshock to the magnetosheath. The observation results are in good agreement with our numerical simulation, which experimentally demonstrates that the reconnecting current sheets downstream of the shock originate from the upstream waves.

RESULTS

Observation overview

Magnetospheric Multiscale (MMS) satellites traversed the bow shock and the magnetosheath from 11:33:00 to 11:39:00 UT on 19 November 2015. Figure 1 shows an overview of the plasma and magnetic field measurements in the Geocentric Solar Ecliptic (GSE) coordinate system. The crossing of the bow shock from the solar wind to the magnetosheath is usually characterized by large increases in the magnetic field strength and plasma density, which are accompanied by decelerated and deflected bulk flow. The jump of magnetic field strength and plasma density from the solar wind to the magnetosheath is consistent on average with the Rankine-Hugoniot relation for the fast mode shock. On the basis of these criteria, the interval in Fig. 1 was divided into three sections: the foreshock from 11:33:00 to 11:35:05 UT, the shock from 11:35:05 to 11:36:15 UT, and the magnetosheath after 11:36:15 UT. The clear shock encounter at approximately 11:35:05 UT (denoted by the first vertical dashed line) can be identified by the rapid changes in the ion energy spectrum (Fig. 1A), plasma density (Fig. 1D), and velocity (Fig. 1E). In the foreshock region upstream of the shock, the average plasma density was 11.0 cm^{-3}, the ion bulk velocity $\boldsymbol{V}_{i0}$ was (−408.3, 38.3, 24.5) km/s, and the magnetic field $\boldsymbol{B}_0$ was (4.48, −0.84, −1.88) nT (the data for 11:33:00 to 11:33:15 UT were used). Downstream of the shock, the magnetosheath was characterized by large-amplitude fluctuations in both the magnetic field and plasma density. Simultaneously, the bulk flow direction deviated from the $-X_{GSE}$ direction to the $-X_{GSE}$ and $+Y_{GSE}$ direction such that the plasma flowed around the magnetosphere, which was also a typical characteristic of the magnetosheath. In the magnetosheath, the average plasma density was 32.4 cm^{-3}, the ion bulk velocity was (−134.3, 148.2, −17.2) km/s, and the magnetic field was (4.15, 9.88, 10.6) nT. The data for 11:36:20 to 11:36:30 UT when the fluctuations were relatively weak were used to estimate the magnetosheath

[1]Deep Space Exploration Laboratory/School of Earth and Space Sciences, University of Science and Technology of China, Hefei, Anhui, China. [2]CAS Center for Excellence in Comparative Planetology/CAS Key Lab of Geospace Environment, University of Science and Technology of China, Hefei, Anhui, China. [3]Collaborative Innovation Center of Astronautical Science and Technology, Harbin, Heilongjiang, China.
*Corresponding author. Email: qmlu@ustc.edu.cn (Q.L.); rswan@ustc.edu.cn (R.W.)
†These authors contributed equally to this work.

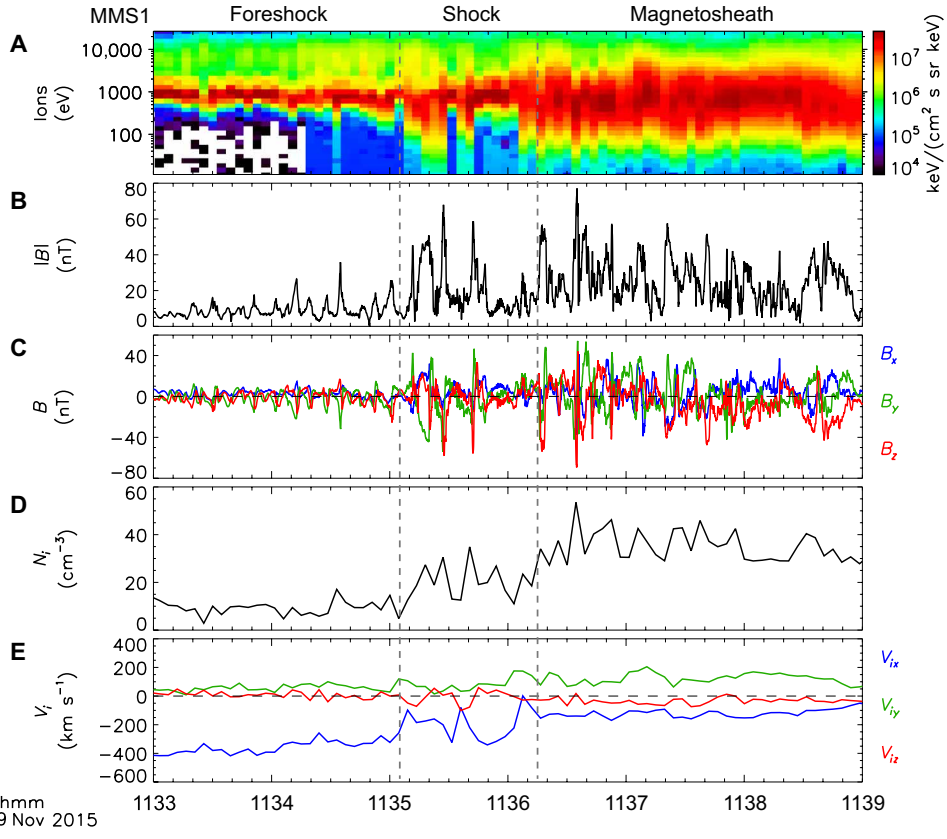

Fig. 1. Overview of MMS1 observations across a quasi-parallel shock. The data are displayed in the GSE coordinate system. (**A**) Ion energy–time spectrogram of differential energy flux. (**B**) Magnitude of the magnetic field. (**C**) Three components (B_x, blue; B_y, green; B_z, red) of the magnetic field. (**D**) Ion number density. (**E**) Three components (V_{ix}, blue; V_{iy}, green; V_{iz}, red) of the ion bulk velocity.

background value. The typical properties of the magnetosheath were observed continuously for about 2.5 hours until approximately 14:00 UT (the observations after 11:39 UT are not shown in Fig. 1). Since the observations by the four MMS satellites are almost identical (fig. S1), only the MMS1 measurements are presented in Fig. 1.

The shock normal angle θ_{Bn}, representing the angle between the upstream magnetic field $\boldsymbol{B}_0$ and the shock normal, was approximately 30° (see Materials and Methods). Therefore, the shock was a quasi-parallel shock. The upstream Alfvén Mach number was 12.4. It should be noted that two distinct ion populations were detected in the upstream foreshock region (11:33:00 to 11:35:05 UT). The lower-energy population (0.4 to 2.5 keV) with a narrower spectrogram corresponded to the incoming solar wind ions, while the higher-energy population (2.5 to 10 keV) represented the backstreaming ions with a propagation direction opposite to that of the incoming solar wind ions. These backstreaming ions were hotter and more tenuous. The solar wind ion β was computed to be 9.6 after subtracting the contribution of the backstreaming population. Throughout the interval shown in Fig. 1, substantial magnetic fluctuations were observed, manifesting as a series of monolithic spikes in both the foreshock and the magnetosheath regions. The amplitude of these magnetic fluctuations increased rapidly as the spacecraft traversed the shock.

Properties and evolution of foreshock waves

Figure 2 (A to D) presents the satellite measurements of the foreshock from 11:33:00 to 11:35:05 UT. To identify the observed plasma wave mode, the spacecraft data were examined in a new local coordinate system *i*-*j*-*k* based on minimum variance analysis (MVA) (*25*), in which three orthogonal eigenvectors ($\boldsymbol{e}_i$, $\boldsymbol{e}_j$, and $\boldsymbol{e}_k$), which represent the directions of the maximum, intermediate, and minimum variance of the magnetic field, respectively, were obtained. The timing analysis (*26*) based on the magnetic fields measured by the four MMS satellites indicates that the waves propagated along the $+\boldsymbol{e}_k$ direction [$\boldsymbol{e}_k = (0.873, -0.002, -0.488)_{GSE}$, i.e., sunward propagation] in the plasma frame, with a phase velocity of 55 km/s, which is ~1.7 times the Alfvén speed V_A (see Materials and Methods). The frequency of the waves in the plasma frame was about 0.014 Hz (~0.187 times the proton gyrofrequency Ω_i), and the corresponding wavelength was 3929 km (~57 ion inertial lengths d_i). The angle between $\boldsymbol{e}_k$ and the upstream magnetic field $\boldsymbol{B}_0$ was 12°, indicating that the foreshock waves propagated mostly parallel to the background magnetic field.

Initially (11:33:00 to 11:33:15 UT), the waves were linear, as shown by the quasi-sinusoidal magnetic fields B_i and B_j variations superimposed on the constant B_k (Fig. 2B). Then, as the satellites approached the shock, the quasi-sinusoidal waveforms changed to phase-steepened waves, which is reflected by a series of solitary

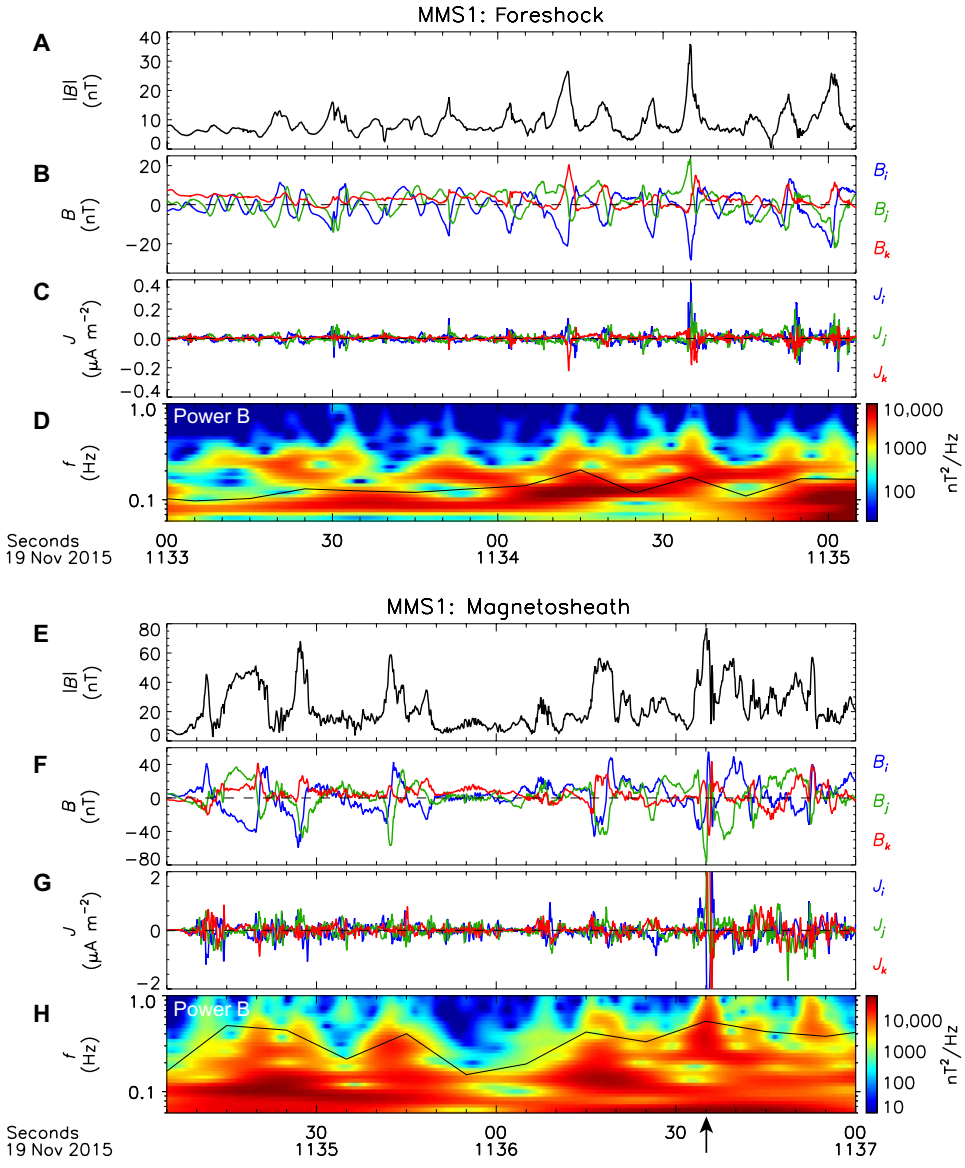

Fig. 2. Measurements in the foreshock and magnetosheath. The data are displayed in an *i-j-k* coordinate system determined from the MVA of the MMS1 magnetic field at 11:33:00 to 11:33:15 UT, with $\boldsymbol{e}_i = (0.099, 0.980, 0.174)_{GSE}$, $\boldsymbol{e}_j = (0.478, -0.200, 0.855)_{GSE}$, and $\boldsymbol{e}_k = (0.873, -0.002, -0.488)_{GSE}$. (**A** and **E**) Magnitude of the magnetic field. (**B** and **F**) Three components (B_i, blue; B_j, green; B_k, red) of the magnetic field. (**C** and **G**) Three components (J_i, blue; J_j, green; J_k, red) of the current density computed from $\nabla \times \boldsymbol{B} / \mu_0$. (**D** and **H**) Wavelet power spectra of the magnetic field. The local proton gyrofrequency is marked by black curves. The interval from 11:35:05 to 11:36:15 UT corresponds to the shock part in Fig. 1; however, this shock transition is composed of a series of large amplitude magnetic pulses that have typical magnetosheath properties. Therefore, this interval is also included in the magnetosheath part in Fig. 2 (E to H), to study their properties.

magnetic field pulses with $B_{max}/|\boldsymbol{B}_0| > 2.0$ (mostly B_i and B_j). After about 11:34:00 UT, B_k no longer remained stable, and it exhibited positive enhancements near the center of the pulses. Figure 2C shows the current density calculated using the curlometer method (*27*), which assumes that the magnetic field has a linear variation across the satellites' separation. The current density within these pulses increased substantially compared to that in the initial quasi-sinusoidal waves, and the currents were in directions both parallel and perpendicular to $\boldsymbol{e}_k$. Figure 2D plots the power spectrum of the magnetic field. It shows that the observed wave frequency in the spacecraft frame remained almost the same (mainly at 0.06 to 0.1 Hz) before 11:34:00 UT, and then, the spectrum exhibited a broadening trend.

To examine the evolution of the amplified magnetic field pulses in the magnetosheath, Fig. 2 (E to H) shows the satellite measurements from 11:35:05 to 11:37:00 UT in the *i-j-k* coordinate system. Each of the pulses exhibited a monolithic pattern in $|\boldsymbol{B}|$ (Fig. 2E). The magnetic field strength was amplified by a factor of 9 or more above the background field, which was much larger than that in the foreshock region. The magnetic field variations in these amplified pulses were sharper, corresponding to larger current densities. The large and narrow spikes of the current density within these pulses

(Fig. 2G) reveal the presence of complex filamentary structures with peak current densities exceeding 0.5 μA/m^2. For these current density spikes, the magnetic field variation was a few tens of nanotesla, implying a width of a few hundreds of kilometers (the ion inertial length d_i was about 40 km in the magnetosheath) based on Ampere's law. These well-separated filamentary currents with small spatial scales and large current densities were potential regions in which magnetic reconnection was initiated. The magnetic field in the magnetosheath had a broader wave spectrum of up to ~1.0 Hz (approximately local proton gyrofrequency) inside each magnetic pulse.

Magnetic reconnection in the magnetosheath

To identify the signatures of magnetic reconnection in magnetosheath current sheets, spacecraft data should be transformed into a current sheet boundary normal (*L-M-N*) coordinate system in which $\boldsymbol{L}$ is oriented along the reconnecting magnetic field direction, $\boldsymbol{N}$ is oriented along the current sheet normal, and $\boldsymbol{M} = \boldsymbol{N} \times \boldsymbol{L}$ is the direction out of the reconnection plane. The primary evidence for the occurrence of magnetic reconnection is bidirectional plasma outflow jets detected on two sides of the reconnection site (*7*, *28*), i.e., bipolar plasma outflow in the *L* direction accompanied by reversal of the normal magnetic field component B_N. The *L-M-N* coordinate system was obtained using a hybrid method (*29*) by combining the results of the MVA and the minimum directional derivative (MDD) (*30*) of the magnetic field (see Materials and Methods).

We examined each thin current sheet shown in Fig. 2 in its *L-M-N* coordinate system and identified two current sheets with direct reconnection signatures. The two current sheets were observed within the magnetic field pulses in the magnetosheath. The current sheet at around 11:36:35 UT (marked with a black arrow at the bottom of Fig. 2) was analyzed in detail to provide evidence of reconnection. All four MMS satellites crossed this current sheet (fig. S2) and detected similar reconnection signatures.

Figure 3 presents the detailed observations of the current sheet at ~11:36:35 UT at MMS1. The timing method indicates that the current sheet moved at a speed of 70 km/s along the normal direction. The duration of the current sheet (11:36:35.1 to 11:36:35.5 UT) was 0.4 s, and thus, its width in the normal direction was 28 km, which corresponds to ~0.8 ion inertial lengths. Inside the current layer, the MMS1 satellite observed a sharp B_L reversal from about 60 nT to about −55 nT between 11:36:35.1 and 11:36:35.5 UT (Fig. 3A), corresponding to the intense current J_M (Fig. 3D), which was supplied by the fast electron flow V_{eM} (Fig. 3C). The electron outflow V_{eL} had a positive value of approximately 200 km/s (~1.2 V_{AiL}) on the positive B_L side and a negative value of approximately −500 km/s (~2.9 V_{AiL}) on the negative B_L side. Here, V_{AiL} is the ion Alfvén speed calculated using the asymptotic B_L and number density of the current sheet. This flow reversal coincided with a change in the normal magnetic field B_N from positive to negative, suggesting that the satellite crossed a reconnection site along the trajectory denoted by the magenta dashed arrow in Fig. 3J.

Figure 3E shows the three components of the electric field in the spacecraft frame. The normal electric field E_N was negative on the positive B_L side, and it became much less negative and occasionally positive after the reversal of B_L; that is, the electric field E_N pointed toward the center of the current sheet, which is illustrated by the orange arrows in Fig. 3J. Furthermore, the energy dissipation in the electron frame (*31*) $\boldsymbol{J} \cdot (\boldsymbol{E} + \boldsymbol{V}_e \times \boldsymbol{B})$ (Fig. 3F) exhibited a positive peak of up to 30 nW/m^3 near the center of the current sheet (marked by the vertical dashed line), indicating strong energy conversion from the magnetic field to the plasma near the reconnection site. The electron temperature increased during the crossing of the current sheet (Fig. 3I), suggesting that the electrons were heated within the current sheet. The electron heating was more notable in the direction parallel to the magnetic field ($\Delta T_{e\|} \approx 16$ eV) than in the direction perpendicular to the magnetic field ($\Delta T_{e\perp} \approx 6$ eV), and the heating predominantly occurred on the positive B_L side.

Figure 3G plots the three components of the magnetic flux transport velocity $\boldsymbol{U}_\psi$ (see Materials and Methods), which is a supplement to the electron outflow for identifying the reconnection site (*32*). $\boldsymbol{U}_\psi$ exhibited a negative-to-positive variation in the *N* direction near the center of the current sheet, corresponding to bidirectional inflows of the magnetic flux when the satellite crossed the current sheet along the $-N$ direction. In addition, $\boldsymbol{U}_\psi$ exhibited a bipolar signature from positive to negative in the *L* direction. The region with large magnetic flux transport flows was much smaller than that characterized by electron outflows. The magnitudes of $\boldsymbol{U}_\psi$ in the inflow and outflow directions were both super-Alfvénic. These bidirectional inflows and outflows of the magnetic flux were consistent with the satellite trajectory through the reconnection site shown in Fig. 3J. The divergence of $\boldsymbol{U}_\psi$ normalized to the local electron gyrofrequency $(\nabla \cdot \boldsymbol{U}_\psi)/f_{ce}$ also exhibited bipolar variation (Fig. 3H), which represents converging inward and diverging outward transports of the magnetic flux at the reconnection site, signifying ongoing magnetic reconnection. Observations of another reconnecting current sheet in the magnetosheath (at ~11:35:20.4 UT) are shown in fig. S3. Although bidirectional electron outflow jets were not observed in this current sheet, the unidirectional super-Alfvénic electron jet also suggests that magnetic reconnection was occurring.

Simulation and comparison with spacecraft observations

To better understand the observational results, in this section, we perform a 2.5-dimensional (2.5D) hybrid simulation of a quasi-parallel shock (see Materials and Methods). The simulation is performed in the *x-y* plane, and the *x* axis is along the Sun-Earth line. In our simulation, the $-x$ direction is the sunward direction. The parameters (plasma β, shock normal angle, and Alfvén Mach number) adopted in the simulation are all chosen to be consistent with the values observed by the MMS satellites. An overview of the simulation results is shown in Fig. 4, in which we plot the magnetic field and in-plane magnetic field lines in the simulation at a representative time, $t = 125\Omega_i^{-1}$. At this time, the shock and foreshock waves are well-developed, and the shock is located at $x \approx 600 d_i$. The solar wind moves antisunward, i.e., in the $+x$ direction. The waves move antisunward along with the solar wind and are amplified, with the magnitude of the magnetic field increasing from $\delta B < B_0$ upstream to $\delta B \sim 5B_0$ downstream.

Using the magnetic field data from the simulation, we perform MVA to obtain the propagation direction of the waves, $\boldsymbol{e}_k = (-0.964, -0.264, 0)_{sim}$, in the *x-y-z* coordinate system of the simulation. The simulation here is 2.5D, and therefore, $\boldsymbol{e}_k$ is confined to the simulation plane, i.e., the *x-y* plane. Because the waves are generated by the backstreaming ions, they propagate upstream, mostly sunward. We perform power spectral analysis to obtain the frequency ω and the wave number $\boldsymbol{k}$ of the waves in the simulation frame (also referred to as the spacecraft frame). The wave power peaks at $\omega = 0.613\Omega_i$ and $k_x d_i = -0.0835$, as shown in fig. S4. Since $\boldsymbol{e}_k$ is the unit vector

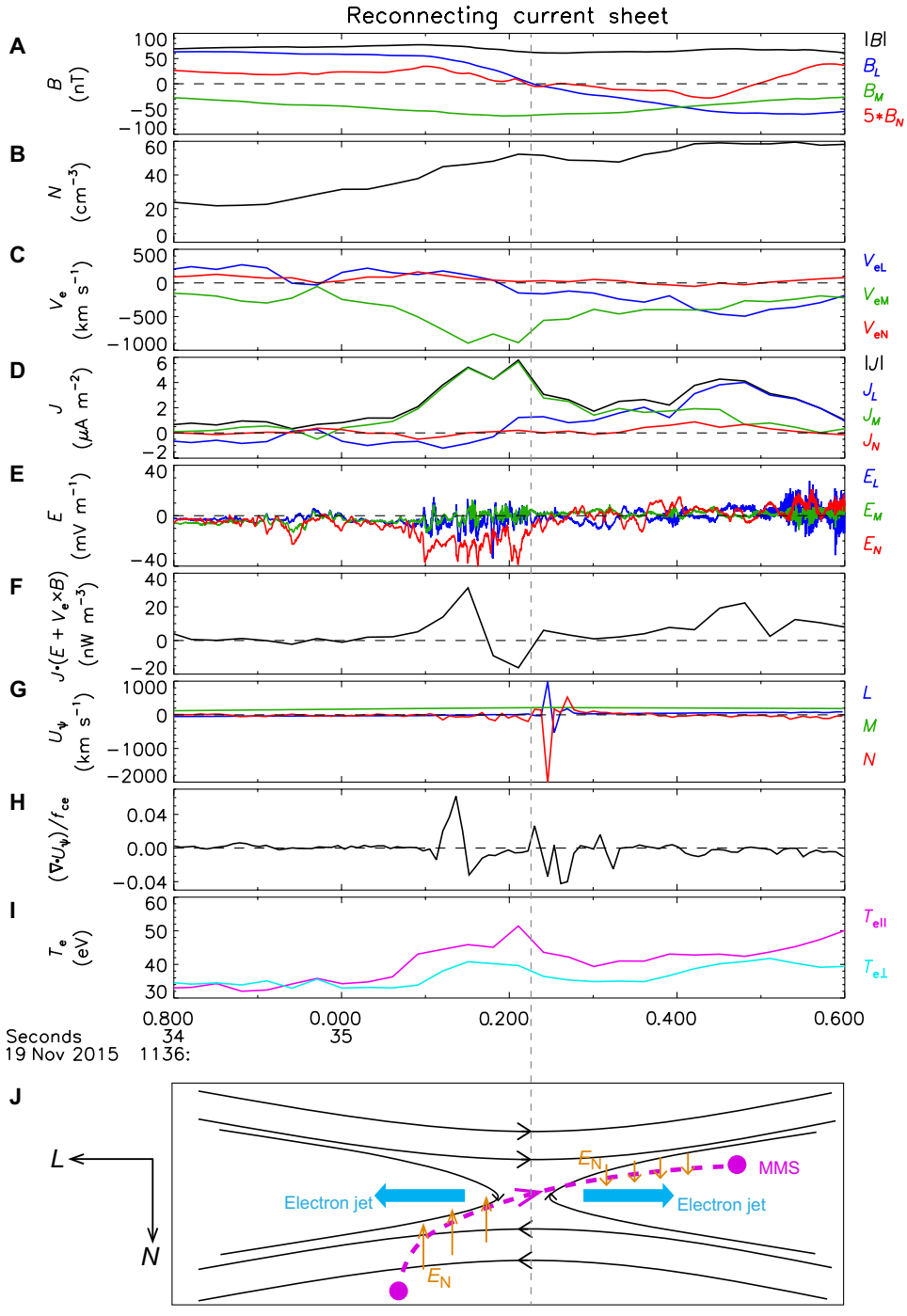

Fig. 3. MMS observations of a reconnecting current sheet in the magnetosheath. The data are displayed in a current sheet boundary normal (*L-M-N*) coordinate system determined from a hybrid method, with $\boldsymbol{L} = (0.070, -0.414, -0.908)_{GSE}$, $\boldsymbol{M} = (0.605, -0.706, 0.369)_{GSE}$, and $\boldsymbol{N} = (-0.793, -0.575, 0.201)_{GSE}$. (**A**) Magnetic field (B_L, blue; B_M, green; B_N amplified to a factor of five, red) and its magnitude (black). (**B**) Electron number density. (**C**) Electron bulk velocity (V_{eL}, blue; V_{eM}, green; V_{eN}, red). (**D**) Current density (J_L, blue; J_M, green; J_N, red) and its magnitude (black). Here, the current density is calculated from $\boldsymbol{J} = N_e e(\boldsymbol{V}_i - \boldsymbol{V}_e)$ where N_e is the electron number density (assuming a quasi-neutral proton plasma), e is the elementary charge, and $\boldsymbol{V}_i$ and $\boldsymbol{V}_e$ are the ion and electron bulk velocities, respectively. The 30-ms electron and 150-ms ion burst data were used. (**E**) Electric field (E_L, blue; E_M, green; E_N, red). (**F**) $\boldsymbol{J} \cdot (\boldsymbol{E} + \boldsymbol{V}_e \times \boldsymbol{B})$. (**G**) Magnetic flux transport velocity $\boldsymbol{U}_\psi$ ($U_{\psi L}$, blue; $U_{\psi M}$, green; $U_{\psi N}$, red). (**H**) The divergence of the magnetic flux transport velocity normalized to the local electron gyrofrequency $(\nabla \cdot \boldsymbol{U}_\psi)/f_{ce}$. (**I**) Electron parallel (magenta) and perpendicular (cyan) temperatures. (**J**) A simplified illustration of the reconnecting current sheet in the *L-N* plane. The black solid lines represent the magnetic fields. The light blue arrows denote the bidirectional electron outflow jets. The orange arrows show the electric field E_N which is directed to the center of the current sheet. The magenta dashed arrow shows a possible spacecraft trajectory through the current sheet from one side of the X-line to the other side. The outflow reversal of V_{eL} from positive to negative accompanied by the change of normal magnetic field B_N from positive to negative was observed by MMS spacecraft during the crossing.

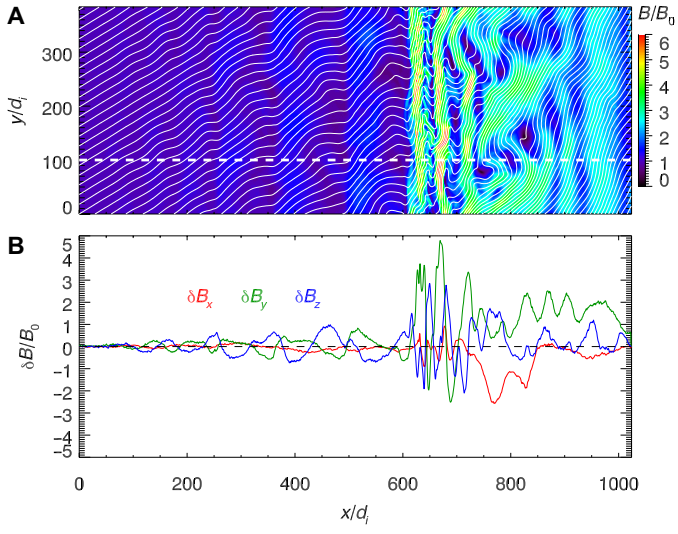

Fig. 4. Hybrid simulation overview. (**A**) Colors show the magnitude of the magnetic field in the simulation domain at a represented time $t = 125\Omega_i^{-1}$; the white curves represent the magnetic field lines in the *x*-*y* plane. (**B**) Profiles of magnetic field fluctuations $\delta B_x = B_x - B_{0x}$ (red), $\delta B_y = B_y - B_{0y}$ (green), and $\delta B_z = B_z - B_{0z} = B_z$ (blue) along $y = 100d_i$ [represented by the white dashed line in (A)].

of $\boldsymbol{k}$, we have $(k_x, k_y, k_z) = (-0.0835, -0.0229, 0)d_i^{-1}$, i.e., $kd_i = 0.0866$. Therefore, in the plasma frame, the wave frequency is $\omega' = \omega + \boldsymbol{k} \cdot \boldsymbol{V}_{sw} = -0.18\Omega_i$. Here, a negative value means that the wave polarization changes in the plasma frame, and the phase velocity of the waves is $|\omega'|/k = 2.08V_A$. The characteristics of the foreshock waves obtained from our simulation are consistent with those in the above MMS observations (table S1). It should be noted that the simulation presented above is 2.5D (2D in space and 3D in velocity space), and we also perform a full 3D (3D in both space and velocity space) simulation and obtain consistent wave characteristics (fig. S5).

Although these waves propagate upstream, their velocity is much lower than the solar wind velocity, causing them to be convected downstream. To better examine the polarization and evolution of these waves, we perform virtual spacecraft observations and transform the data from the *x*-*y*-*z* simulation coordinate system into an *i*-*j*-*k* coordinate system, where $\boldsymbol{e}_k = (-0.964, -0.264, 0)_{sim}$ is the propagation direction of the waves. For convenience, we choose $\boldsymbol{e}_i = (0, 0, 1)_{sim}$ as the first transverse direction, and thus, $\boldsymbol{e}_j = (-0.264, 0.964, 0)_{sim}$ is the other transverse direction. Figure 5 shows a side-by-side comparison between the virtual spacecraft observations and the MMS observations. In the far foreshock, the waves are linear and sinusoidal (Fig. 5, A and G). In the MMS/virtual spacecraft frame, the waves propagate along with the solar wind, i.e., predominantly antisunward in the $-k$ direction. Therefore, in the spacecraft frame, the anticlockwise hodograms show that the waves are left-handed circularly polarized (Fig. 5, B and H). We have shown above that the polarization changes from the spacecraft frame to the plasma frame. Therefore, the waves are right-handed polarized in the plasma frame. The frequency, phase velocity, and polarization of these waves support the conclusion that they are right-handed resonant fast magnetosonic waves, as shown in previous studies (*19*, *33*, *34*).

The waves become nonlinear and amplified as they are convected toward the near foreshock, and the transverse components, δB_i and δB_j, become in-phase, exhibiting highly elliptical or even linear polarization (Fig. 5, C, D, I, and J). After the shock, the waves are transformed into intermittent structures, i.e., current sheets and even reconnection therein, and the magnetic field components are further amplified and highly fluctuating (Fig. 5, E, F, K, and L).

The foreshock waves are compressed by the shock and become highly fluctuating in the magnetosheath, forming current sheets. Magnetic reconnection occurs in these current sheets, and Fig. 6 shows the occurrence of magnetic reconnection in one of them. At $t = 92\Omega_i^{-1}$, a long, thin current sheet is formed at around $(x, y) = (750, 100)d_i$ (Fig. 6A). At $t = 96\Omega_i^{-1}$, the topological change in the magnetic field lines shows the occurrence of magnetic reconnection at $(x, y) = (749, 91.3)d_i$ (Fig. 6B). The reconnection site is a null point, which is usually referred to as the X point. Because of the topological changes caused by magnetic reconnection, another null point, the O point, is formed at $(x, y) = (755.5, 81.4)d_i$. The reconnected magnetic flux, i.e., the difference between the magnetic flux ψ at the X and O points, is $1.33B_0d_i$. At $t = 100\ \Omega_i^{-1}$ (Fig. 6C), the X point is located at $(x, y) = (747.1, 86.4)d_i$, the O point is located at $(x, y) = (757.9, 75.4)d_i$, and the reconnected magnetic flux increases to $2.94B_0d_i$, which shows that active magnetic reconnection is ongoing at the X point. Moreover, the occurrence of magnetic reconnection in the turbulent magnetosheath is also found in our full 3D simulation (fig. S6). Note that the high-frequency turbulence related to electron dynamics which has been investigated by particle-in-cell simulations (*35*–*37*) cannot be resolved in the hybrid simulations.

DISCUSSION

By presenting spacecraft observations and numerical simulations, we provide persuasive evidence that the fast magnetosonic waves upstream of the Earth's bow shock can transmit through the shock and form thin current sheets in the turbulent downstream magnetosheath. Last, magnetic reconnection is triggered in such thin current sheets. These reconnecting current sheets do not necessarily have the same characteristics, some showing the typical Hall reconnection features (*9*) whereas some others showing electron dynamics without the coupling of ions (*7*). This is relevant to the different spatial scales of the current sheets that are originated from different nonlinearities in the turbulence (*10*). The nonlinear effects lead to the formation of current sheets with not only different spatial scales but also different plasma and magnetic configurations, especially different guide fields perpendicular to the reconnection plane, which can also affect the reconnection characteristics by modifying the particle dynamics during the magnetic reconnection (*38*–*41*). Therefore, the turbulent magnetosheath hosts magnetic reconnection with various types of characteristics, which renders the magnetosheath even more turbulent.

In addition to the foreshock-shock-magnetosheath system, our results can be generalized to many other shocked and turbulent plasmas in various astrophysical and laboratorial environments, such as supernova remnant shocks (*42*), the heliospheric termination shock (*43*), coronal mass ejections (*44*), and laser-produced plasma experiments (*45*), which provides a viable formation mechanism for coherent current sheets that precondition magnetic reconnection in them. Because magnetic reconnection can dissipate magnetic energy to enable efficient particle energization, this

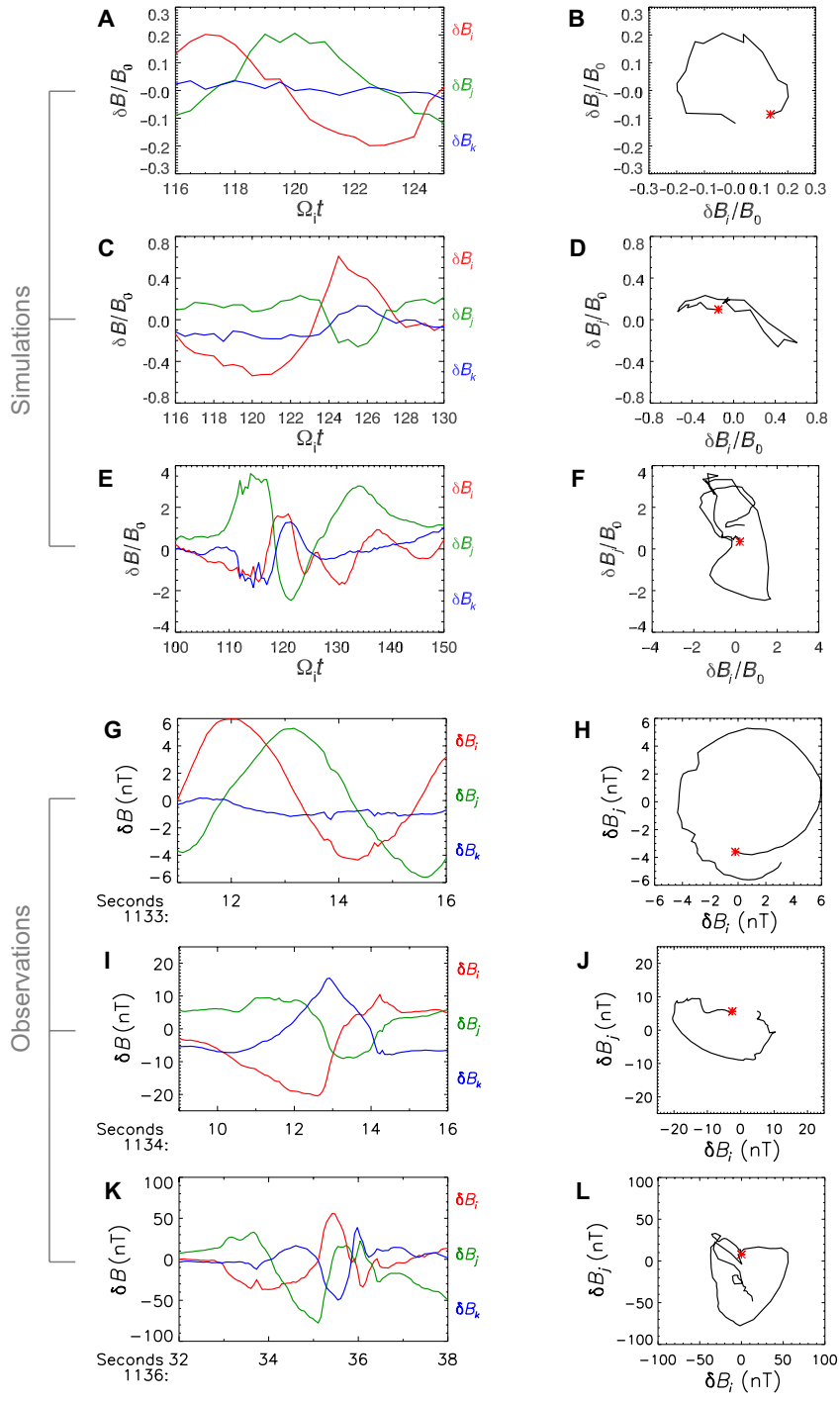

Fig. 5. Comparison between hybrid simulations and MMS observations. Magnetic fluctuations in the *i-j-k* coordinate systems, δB_i (red), δB_j (green), and δB_k (blue), in both simulations and observations. In the simulations (from the first to the third row), $\boldsymbol{e}_i = (0, 0, 1)$, $\boldsymbol{e}_j = (-0.264, 0.964, 0)$, and $\boldsymbol{e}_k = (-0.964, -0.264, 0)$ in the simulation *x-y-z* coordinate system. In the observations (from the fourth to the sixth row), $\boldsymbol{e}_i = (0.099, 0.980, 0.174)$, $\boldsymbol{e}_j = (0.478, -0.200, 0.855)$, and $\boldsymbol{e}_k = (0.873, -0.002, -0.488)$ in the GSE coordinate system. The simulation results are presented as virtual spacecraft observations. (**A** and **B**) At $(x, y) = (100, 100)d_i$ in the far foreshock, (**C** and **D**) at $(x, y) = (250, 100)d_i$ in the near foreshock, and (**E** and **F**) along the trajectory of $x = 650d_i + 2V_A(t - 100\Omega_i^{-1})$ and $y = 100d_i$ in the magnetosheath. Here, in the far and near foreshock, the virtual spacecraft does not move relative to the simulation domain because it can well observe the spatial structures that move along with the solar wind. On the other hand, in the magnetosheath, because the structures therein move much slower than those in the solar wind, to allow the virtual spacecraft to observe the structures in the magnetosheath, we let the virtual spacecraft move (along the above trajectory) at a relative velocity. (A, C, and E) Time history of the magnetic fluctuations. [(B), (D), and (F)] Hodograms of the magnetic fluctuations in the δB_i-δB_j plane, corresponding to the intervals in (A), (C), and (E), respectively. The MMS spacecraft observations are shown in (G) to (L). (**G**, **I**, and **K**) Time series of the magnetic fluctuations. (**H**, **J**, and **L**) Hodograms of the magnetic fluctuations, corresponding to the intervals in (G), (I), and (K), respectively. The red star on the trace represents the beginning of the interval.

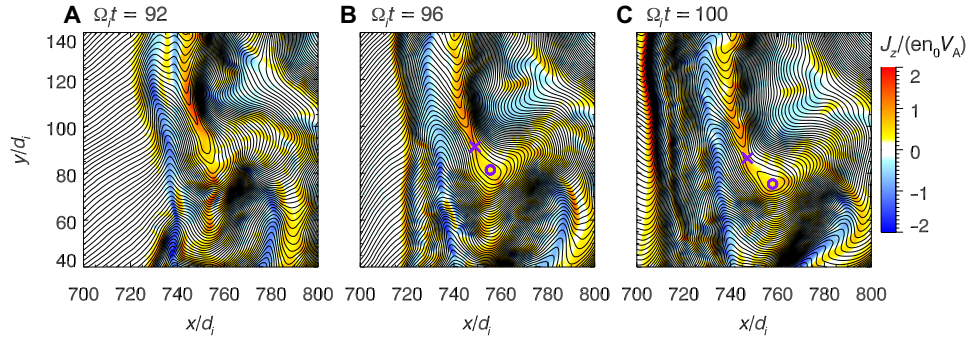

Fig. 6. Reconnecting magnetosheath current sheet in the hybrid simulation. In a zoomed-in region in the magnetosheath, colors show the out-of-plane current density in the *z* direction, J_z, in unit of en_0V_A; and the black curves represent the magnetic field lines in the *x*-*y* plane at t = (**A**) $92\Omega_i^{-1}$, (**B**) $96\Omega_i^{-1}$, and (**C**) $100\Omega_i^{-1}$. In (B) and (C), the purple cross and circle marks represent the X point and O point, respectively.

mechanism can have important implications for explaining energy cascade, radio bursts, and cosmic-ray acceleration resulting from turbulent magnetic reconnection in these environments (*46*, *47*).

MATERIALS AND METHODS

Determination of the shock normal angle

The shock normal angle θ_{Bn} is the angle between the upstream magnetic field $\boldsymbol{B}_0$ and the shock normal $\boldsymbol{n}$. Two methods were used to estimate the shock normal $\boldsymbol{n}$. One is based on the analytical shape of the shock according to a large number of previous spacecraft encounters. These statistical datasets can be fit by geometrical forms, from which the shock normal can be computed analytically. We used the model of Farris *et al.* (*48*) and calculated the shock angle θ_{Bn} to be 31°. The other method is based on the coplanarity theorem, in which the flow, magnetic field, and shock normal on both sides of the shock all lie in the same plane. Thus, there are a variety of vectors that lie in the shock plane. The shock normal can be obtained by the cross-product of two such vectors. Here, we used $\boldsymbol{n} = [(\Delta\boldsymbol{B} \times \Delta\boldsymbol{V}) \times \Delta\boldsymbol{B}]/\,|(\Delta\boldsymbol{B} \times \Delta\boldsymbol{V}) \times \Delta\boldsymbol{B}|$, where Δ indicates the jump (downstream minus upstream) in the quantity, i.e., $\Delta\boldsymbol{B} \equiv \boldsymbol{B}_d - \boldsymbol{B}_u$ and $\Delta\boldsymbol{V} \equiv \boldsymbol{V}_d - \boldsymbol{V}_u$, and we calculated the shock angle θ_{Bn} to be 28°. Therefore, the results of both methods indicate that the shock in this event was a quasi-parallel shock.

Propagation of foreshock waves

For circularly polarized waves, the MVA (*25*) can obtain the propagation direction of the waves but with a 180° ambiguity. MVA was performed to the MMS1 magnetic field of the interval 11:33:00 to 11:33:15 UT, by which three orthogonal eigenvectors ($\boldsymbol{e}_i$, $\boldsymbol{e}_j$, and $\boldsymbol{e}_k$) representing the directions of maximum, intermediate, and minimum variance of the magnetic field were obtained. Here, $\boldsymbol{e}_k = (0.873, -0.002, -0.488)_{\mathrm{GSE}}$ was adjusted to make it sunward, and it is considered to be parallel or antiparallel to the direction of wave propagation. To determine the true propagation direction in the spacecraft frame, the timing method (*26*) based on the magnetic fields measured by four MMS satellites was used. We calculated the propagation velocity of the observed waves in 11:33:00 to 11:34:00 UT to be 313 km/s along the $-\boldsymbol{e}_k$ direction, indicating that the waves propagated antisunward in the spacecraft frame. The velocity of the solar wind was (1.4, −181.8, −368.4) km/s in the *i*-*j*-*k* coordinate system. Therefore, in the plasma frame, the wave phase velocity was 55 km/s (~1.7V_A) along the $+\boldsymbol{e}_k$ direction, propagating sunward.

Determination of the *L*-*M*-*N* coordinate system for a current sheet

We used a hybrid method (*29*) to determine the *L*-*M*-*N* coordinate system for a current sheet. This method combines the maximum variance direction of the magnetic field ($\boldsymbol{e}'_L$) from MVA and the maximum gradient direction of the magnetic field ($\boldsymbol{e}'_N$) from MDD (*30*) and then rotates these directions to be perpendicular. First, we defined $\boldsymbol{e}_M \equiv \boldsymbol{e}'_N \times \boldsymbol{e}'_L$ and $\boldsymbol{e}''_L \equiv \boldsymbol{e}_M \times \boldsymbol{e}'_N$. Next, we calculated the angle θ between $\boldsymbol{e}'_L$ and $\boldsymbol{e}'_N$ and defined $\theta' \equiv \theta - 90^{\circ}$. Define the ratio of maximum and intermediate eigenvalues from MVA and MDD as λ_1 and λ_2, respectively. The rotation angle from $\boldsymbol{e}'_N$ to $\boldsymbol{e}''_L$ is $d\theta = \theta'\,\lambda_1/(\lambda_1 + \lambda_2)$. Then, $\boldsymbol{e}_N = \cos(d\theta)\boldsymbol{e}'_N + \sin(d\theta)\boldsymbol{e}''_L$. Last, complete the coordinate system with $\boldsymbol{e}_L = \boldsymbol{e}_M \times \boldsymbol{e}_N$.

The computation of magnetic flux transport velocity $\boldsymbol{U}_\psi$

The identification of magnetic reconnection based on the analysis of magnetic flux transport has been studied by Li *et al.* (*32*) and Qi *et al.* (*49*). The bidirectional inflows and outflows of magnetic flux around a reconnection site suggest that reconnection is ongoing. The formula of the magnetic flux transport velocity $\boldsymbol{U}_\psi$ (*32*) in the 2D case is

$$\boldsymbol{U}_\psi \equiv \boldsymbol{V}_{ep} - (\boldsymbol{V}_{ep} \cdot \boldsymbol{b}_\mathrm{p})\boldsymbol{b}_\mathrm{p} + E'_{eM}(\boldsymbol{M} \times \boldsymbol{b}_\mathrm{p})/B_\mathrm{p} \quad (1)$$

where $\boldsymbol{V}_{ep}$ is the in-plane (reconnection *L*-*N* plane) electron flow, $\boldsymbol{b}_p$ is the unit vector of the in-plane magnetic field $\boldsymbol{B}_p$, $\boldsymbol{M}$ is the direction out of the reconnection *L*-*N* plane, and $\boldsymbol{E}'_e = \boldsymbol{E} + \boldsymbol{V}_e \times \boldsymbol{B}$ is the non-ideal electric field in the electron frame. The first two terms represent the in-plane electron flow perpendicular to $\boldsymbol{B}_p$. The last term represents the slippage between magnetic flux and electron flow when $\boldsymbol{E}'_e \neq 0$. Without separating the perpendicular electron flow and slippage terms, which provide a relation between the transport of magnetic flux and electron flow, Eq. 1 can be simplified to

$$\boldsymbol{U}_\psi = (E_M / B_\mathrm{p})(\boldsymbol{M} \times \boldsymbol{b}_\mathrm{p}) \quad (2)$$

Note that magnetic flux generation or annihilation is not included in Eqs. 1 and 2. Here, we used the data averaged over four MMS satellites to calculate $\boldsymbol{U}_\psi$. The ion bulk velocity was subtracted from

$\boldsymbol{U}_\psi$ to show the magnetic flux transport more clearly. An active reconnection site is characterized by super-Alfvénic inflow and outflow flux transport velocity.

Hybrid simulation model

Here, we use a hybrid simulation model. The simulation is 2D in space and 3D in velocity space, and the electric and magnetic fields, velocities, and displacements are 3D. Such simulation is usually referred to as 2.5D. In our hybrid simulation model, the ions are treated as macroparticles, and electrons are treated as a massless fluid. The ions are pushed by solving the equation of motion, the velocity of the electron fluid is calculated using Ampere's law, the momentum equation of the electron fluid is used to calculate the electric field, and the magnetic field is updated by Faraday's law. The simulation is performed in the x-y plane in a domain of $[0, L_x] \times [0, L_y]$, and $\partial/\partial z = 0$ for the out-of-plane direction. The initial plasma density n_0, temperature T_0, and magnetic field B_0 are uniform, and the initial ion and electron plasma β is 9.6. We use a grid number of 2048×768, and the grid size is $\Delta x = \Delta y = 0.5 d_i$, where d_i is the ion inertial length evaluated using n_0. Therefore, we have $L_x = 1024 d_i$ and $L_y = 384 d_i$. The time step is $\Delta t = 0.01 \Omega_i^{-1}$, where Ω_i is the ion gyrofrequency evaluated using B_0. An average of 100 ion particles per grid cell is used at the initial time. The x boundaries are fixed on the basis of the Rankine-Hugoniot condition, and the y boundaries are periodic. The plasmas are injected into the simulation domain from the $x = 0$ boundary at a super-Alfvénic velocity $V_{\rm inj}$ and are reflected at the $x = L_x$ boundary. The interaction between the injected and reflected plasmas forms a shock that propagates in the $-x$ direction. The initial magnetic field $\boldsymbol{B}_0$ is in the x-y plane, with the angle between the magnetic field and the x axis $\theta_{Bx} = 30°$, and therefore, θ_{Bn} is also 30°, i.e., $B_{0x} = 0.866 B_0$, $B_{0y} = 0.5 B_0$, and $B_{0z} = 0$. We set $V_{\rm inj} = 9.5 V_{\rm A}$, where $V_{\rm A}$ is the Alfvén velocity evaluated using B_0 and n_0. The velocity of the shock front is approximately $2.6 V_{\rm A}$; therefore, the Alfvén Mach number of this shock is about 12.1. We also perform a full 3D (3D in both space and velocity space) hybrid simulation to compare with the 2.5D simulation. In the 3D simulation, $V_{\rm inj} = 8.5 V_{\rm A}$, $\Delta x = 0.5 d_i$, $\Delta y = \Delta z = 1.0 d_i$, $L_x = 1024 d_i$, $L_y = 384 d_i$, $L_z = 256 d_i$, and $\Delta t = 0.04 \Omega_i^{-1}$. The rest parameters are identical to those used in the 2.5D simulation.

Supplementary Materials

This PDF file includes:

Figs. S1 to S6
Table S1

REFERENCES AND NOTES

1. C. H. K. Chen, S. Boldyrev, Nature of kinetic scale turbulence in the earth's magnetosheath. *Astrophys. J.* **842**, 122 (2017).
2. F. Sahraoui, G. Belmont, L. Rezeau, N. Cornilleau-Wehrlin, J. L. Pinçon, A. Balogh, Anisotropic turbulent spectra in the terrestrial magnetosheath as seen by the cluster spacecraft. *Phys. Rev. Lett.* **96**, 075002 (2006).
3. E. Yordanova, A. Vaivads, M. André, S. C. Buchert, Z. Vörös, Magnetosheath plasma turbulence and its spatiotemporal evolution as observed by the cluster spacecraft. *Phys. Rev. Lett.* **100**, 205003 (2008).
4. M. Yamada, R. Kulsrud, H. T. Ji, Magnetic reconnection. *Rev. Mod. Phys.* **82**, 603–664 (2010).
5. A. Chasapis, W. H. Matthaeus, T. N. Parashar, O. LeContel, A. Retinò, H. Breuillard, Y. Khotyaintsev, A. Vaivads, B. Lavraud, E. Eriksson, T. E. Moore, J. L. Burch, R. B. Torbert, P. A. Lindqvist, R. E. Ergun, G. Marklund, K. A. Goodrich, F. D. Wilder, M. Chutter, J. Needell, D. Rau, I. Dors, C. T. Russell, G. Le, W. Magnes, R. J. Strangeway, K. R. Bromund, H. K. Leinweber, F. Plaschke, D. Fischer, B. J. Anderson, C. J. Pollock, B. L. Giles, W. R. Paterson, J. Dorelli, D. J. Gershman, L. Avanov, Y. Saito, Electron heating at kinetic scales in magnetosheath turbulence. *Astrophys. J.* **836**, 247 (2017).
6. A. Chasapis, A. Retinò, F. Sahraoui, A. Vaivads, Y. V. Khotyaintsev, D. Sundkvist, A. Greco, L. Sorriso-Valvo, P. Canu, Thin current sheets and associated electron heating in turbulent space plasma. *Astrophys. J. Lett.* **804**, L1 (2015).
7. T. D. Phan, J. P. Eastwood, M. A. Shay, J. F. Drake, B. U. Ö. Sonnerup, M. Fujimoto, P. A. Cassak, M. Øieroset, J. L. Burch, R. B. Torbert, A. C. Rager, J. C. Dorelli, D. J. Gershman, C. Pollock, P. S. Pyakurel, C. C. Haggerty, Y. Khotyaintsev, B. Lavraud, Y. Saito, M. Oka, R. E. Ergun, A. Retino, O. Le Contel, M. R. Argall, B. L. Giles, T. E. Moore, F. D. Wilder, R. J. Strangeway, C. T. Russell, P. A. Lindqvist, W. Magnes, Electron magnetic reconnection without ion coupling in earth's turbulent magnetosheath. *Nature* **557**, 202–206 (2018).
8. T. D. Phan, G. Paschmann, C. Twitty, F. S. Mozer, J. T. Gosling, J. P. Eastwood, M. Øieroset, H. Rème, E. A. Lucek, Evidence for magnetic reconnection initiated in the magnetosheath. *Geophys. Res. Lett.* **34**, L14104 (2007).
9. A. Retinò, D. Sundkvist, A. Vaivads, F. Mozer, M. André, C. J. Owen, In situ evidence of magnetic reconnection in turbulent plasma. *Nat. Phys.* **3**, 235–238 (2007).
10. J. E. Stawarz, J. P. Eastwood, T. D. Phan, I. L. Gingell, P. S. Pyakurel, M. A. Shay, S. L. Robertson, C. T. Russell, O. Le Contel, Turbulence-driven magnetic reconnection and the magnetic correlation length: Observations from magnetospheric multiscale in earth's magnetosheath. *Phys. Plasmas* **29**, 012302 (2022).
11. J. E. Stawarz, J. P. Eastwood, T. D. Phan, I. L. Gingell, M. A. Shay, J. L. Burch, R. E. Ergun, B. L. Giles, D. J. Gershman, O. Le Contel, P.-A. Lindqvist, C. T. Russell, R. J. Strangeway, R. B. Torbert, M. R. Argall, D. Fischer, W. Magnes, L. Franci, Properties of the turbulence associated with electron-only magnetic reconnection in earth's magnetosheath. *Astrophys. J. Lett.* **877**, L37 (2019).
12. D. Sundkvist, A. Retinò, A. Vaivads, S. D. Bale, Dissipation in turbulent plasma due to reconnection in thin current sheets. *Phys. Rev. Lett.* **99**, 025004 (2007).
13. Z. Vörös, E. Yordanova, A. Varsani, K. J. Genestreti, Y. V. Khotyaintsev, W. Li, D. B. Graham, C. Norgren, R. Nakamura, Y. Narita, F. Plaschke, W. Magnes, W. Baumjohann, D. Fischer, A. Vaivads, E. Eriksson, P. A. Lindqvist, G. Marklund, R. E. Ergun, M. Leitner, M. P. Leubner, R. J. Strangeway, O. Le Contel, C. Pollock, B. J. Giles, R. B. Torbert, J. L. Burch, L. A. Avanov, J. C. Dorelli, D. J. Gershman, W. R. Paterson, B. Lavraud, Y. Saito, MMS observation of magnetic reconnection in the turbulent magnetosheath. *J. Geophys. Res.* **122**, 11442–11467 (2017).
14. S. M. Wang, R. S. Wang, Q. M. Lu, J. L. Burch, S. Wang, Energy dissipation via magnetic reconnection within the coherent structures of the magnetosheath turbulence. *J. Geophys. Res.* **126**, e2020JA028860 (2021).
15. E. Yordanova, Z. Vörös, A. Varsani, D. B. Graham, C. Norgren, Y. V. Khotyaintsev, A. Vaivads, E. Eriksson, R. Nakamura, P. A. Lindqvist, G. Marklund, R. E. Ergun, W. Magnes, W. Baumjohann, D. Fischer, F. Plaschke, Y. Narita, C. T. Russell, R. J. Strangeway, O. Le Contel, C. Pollock, R. B. Torbert, B. J. Giles, J. L. Burch, L. A. Avanov, J. C. Dorelli, D. J. Gershman, W. R. Paterson, B. Lavraud, Y. Saito, Electron scale structures and magnetic reconnection signatures in the turbulent magnetosheath. *Geophys. Res. Lett.* **43**, 5969–5978 (2016).
16. W. Daughton, V. Roytershteyn, H. Karimabadi, L. Yin, B. J. Albright, B. Bergen, K. J. Bowers, Role of electron physics in the development of turbulent magnetic reconnection in collisionless plasmas. *Nat. Phys.* **7**, 539–542 (2011).
17. S. Lu, V. Angelopoulos, A. V. Artemyev, P. L. Pritchett, J. Liu, A. Runov, A. Tenerani, C. Shi, M. Velli, Turbulence and particle acceleration in collisionless magnetic reconnection: Effects of temperature inhomogeneity across pre-reconnection current sheet. *Astrophys. J.* **878**, 109 (2019).
18. J. P. Eastwood, E. A. Lucek, C. Mazelle, K. Meziane, Y. Narita, J. Pickett, R. A. Treumann, The foreshock. *Space Sci. Rev.* **118**, 41–94 (2005).
19. S. P. Gary, Electromagnetic ion/ion instabilities and their consequences in space plasmas: A review. *Space Sci. Rev.* **56**, 373–415 (1991).
20. L. Turc, O. W. Roberts, D. Verscharen, A. P. Dimmock, P. Kajdič, M. Palmroth, Y. Pfau-Kempf, A. Johlander, M. Dubart, E. K. J. Kilpua, J. Soucek, K. Takahashi, N. Takahashi, M. Battarbee, U. Ganse, Transmission of foreshock waves through earth's bow shock. *Nat. Phys.* **19**, 78–86 (2023).
21. N. Bessho, L.-J. Chen, S. Wang, M. Hesse, L. B. Wilson III, J. Ng, Magnetic reconnection and kinetic waves generated in the earth's quasi-parallel bow shock. *Phys. Plasmas* **27**, 092901 (2020).
22. H. Karimabadi, V. Roytershteyn, H. X. Vu, Y. A. Omelchenko, J. Scudder, W. Daughton, A. Dimmock, K. Nykyri, M. Wan, D. Sibeck, M. Tatineni, A. Majumdar, B. Loring, B. Geveci, The link between shocks, turbulence, and magnetic reconnection in collisionless plasmas. *Phys. Plasmas* **21**, 062308 (2014).
23. Q. M. Lu, H. Y. Wang, X. Y. Wang, S. Lu, R. S. Wang, X. L. Gao, S. Wang, Turbulence-driven magnetic reconnection in the magnetosheath downstream of a quasi-parallel shock: A three-dimensional global hybrid simulation. *Geophys. Res. Lett.* **47**, e2019GL085661 (2020).
24. Q. M. Lu, A. Guo, Z. Yang, R. Wang, S. Lu, R. Chen, X. Gao, Upstream plasma waves and downstream magnetic reconnection at a reforming quasi-parallel shock. *Astrophys. J.* **964**, 33 (2024).

25. B. U. Sonnerup, L. J. Cahill, Magnetopause structure and attitude from explorer 12 observations. *J. Geophys. Res.* **72**, 171–183 (1967).
26. S. J. Schwartz, Shock and discontinuity normals, mach numbers, and related parameters. *ISSI Sci. Rep. Ser.* **1**, 249–270 (1998).
27. M. W. Dunlop, A. Balogh, K.-H. Glassmeier, P. Robert, Four-point cluster application of magnetic field analysis tools: The curlometer. *J. Geophys. Res.* **107**, 1384 (2002).
28. Q. M. Lu, H. S. Fu, R. S. Wang, S. Lu, Collisionless magnetic reconnection in the magnetosphere. *Chinese Phys. B* **31**, 089401 (2022).
29. R. E. Denton, B. U. Ö. Sonnerup, C. T. Russell, H. Hasegawa, T. D. Phan, R. J. Strangeway, B. L. Giles, R. E. Ergun, P. A. Lindqvist, R. B. Torbert, J. L. Burch, S. K. Vines, Determining *L-M-N* current sheet coordinates at the magnetopause from magnetospheric multiscale data. *J. Geophys. Res.* **123**, 2274–2295 (2018).
30. Q. Q. Shi, C. Shen, Z. Y. Pu, M. W. Dunlop, Q. G. Zong, H. Zhang, C. J. Xiao, Z. X. Liu, A. Balogh, Dimensional analysis of observed structures using multipoint magnetic field measurements: Application to cluster. *Geophys. Res. Lett.* **32**, L12105 (2005).
31. S. Zenitani, M. Hesse, A. Klimas, M. Kuznetsova, New measure of the dissipation region in collisionless magnetic reconnection. *Phys. Rev. Lett.* **106**, 195003 (2011).
32. T. C. Li, Y. H. Liu, Y. Qi, Identification of active magnetic reconnection using magnetic flux transport in plasma turbulence. *Astrophys. J. Lett.* **909**, L28 (2021).
33. J. P. Eastwood, A. Balogh, M. W. Dunlop, T. S. Horbury, I. Dandouras, Cluster observations of fast magnetosonic waves in the terrestrial foreshock. *Geophys. Res. Lett.* **29**, 2046 (2002).
34. Y. F. Hao, Q. M. Lu, D. J. Wu, S. Lu, L. Xiang, Y. G. Ke, Low-frequency waves upstream of quasi-parallel shocks: Two-dimensional hybrid simulations. *Astrophys. J.* **915**, 64 (2021).
35. C. Huang, Q. M. Lu, F. Guo, M. Y. Wu, A. du, S. Wang, Magnetic islands formed due to the kelvin-helmholtz instability in the outflow region of collisionless magnetic reconnection. *Geophys. Res. Lett.* **42**, 7282–7286 (2015).
36. P. A. Muñoz, J. Büchner, Kinetic turbulence in fast three-dimensional collisionless guide-field magnetic reconnection. *Phys. Rev. E* **98**, 043205 (2018).
37. V. Zharkova, Q. Xia, Kinetic plasma turbulence generated an a 3D current sheet with magnetic islands. *Front. Astron. Space Sci.* **8**, 178 (2021).
38. X. R. Fu, Q. M. Lu, S. Wang, The process of electron acceleration during collisionless magnetic reconnection. *Phys. Plasmas* **13**, 012309 (2006).
39. P. L. Pritchett, F. V. Coroniti, Three-dimensional collisionless magnetic reconnection in the presence of a guide field. *J. Geophys. Res.* **109**, A01220 (2004).
40. V. V. Zharkova, K. Arzner, A. O. Benz, P. Browning, C. Dauphin, A. G. Emslie, L. Fletcher, E. P. Kontar, G. Mann, M. Onofri, V. Petrosian, R. Turkmani, N. Vilmer, L. Vlahos, Recent advances in understanding particle acceleration processes in solar flares. *Space Sci. Rev.* **159**, 357–420 (2011).
41. V. V. Zharkova, O. V. Khabarova, Particle dynamics in the reconnecting heliospheric current sheet: Solar wind data versus three-dimensional particle-in-cell simulations. *Astrophys. J.* **752**, 35 (2012).
42. E. G. Berezhko, L. T. Ksenofontov, H. J. Völk, Confirmation of strong magnetic field amplification and nuclear cosmic ray Acceleration in Sn 1006. *Astron. Astrophys.* **412**, L11–L14 (2003).
43. J. D. Richardson, L. F. Burlaga, The solar wind in the outer heliosphere and heliosheath. *Space Sci. Rev.* **176**, 217–235 (2013).
44. E. Kilpua, H. E. J. Koskinen, T. I. Pulkkinen, Coronal mass ejections and their sheath regions in interplanetary space. *Living Rev. Sol. Phys.* **14**, 5 (2017).
45. J. Meinecke, H. W. Doyle, F. Miniati, A. R. Bell, R. Bingham, R. Crowston, R. P. Drake, M. Fatenejad, M. Koenig, Y. Kuramitsu, C. C. Kuranz, D. Q. Lamb, D. Lee, M. J. MacDonald, C. D. Murphy, H.-S. Park, A. Pelka, A. Ravasio, Y. Sakawa, A. A. Schekochihin, A. Scopatz, P. Tzeferacos, W. C. Wan, N. C. Woolsey, R. Yurchak, B. Reville, G. Gregori, Turbulent amplification of magnetic fields in laboratory laser-produced shock waves. *Nat. Phys.* **10**, 520–524 (2014).
46. Y. Matsumoto, T. Amano, T. N. Kato, M. Hoshino, Stochastic electron acceleration during spontaneous turbulent reconnection in a strong shock wave. *Science* **347**, 974–978 (2015).
47. G. P. Zank, P. Hunana, P. Mostafavi, J. A. Le Roux, G. Li, G. M. Webb, O. Khabarova, A. Cummings, E. Stone, R. Decker, Diffusive shock acceleration and reconnection acceleration processes. *Astrophys. J.* **814**, 137 (2015).
48. M. H. Farris, S. M. Petrinec, C. T. Russell, The thickness of the magnetosheath: Constraints on the polytropic index. *Geophys. Res. Lett.* **18**, 1821–1824 (1991).
49. Y. Qi, T. Chu Li, C. T. Russell, R. E. Ergun, Y. D. Jia, M. Hubbert, Magnetic flux transport identification of active reconnection: MMS observations in earth's magnetosphere. *Astrophys. J. Lett.* **926**, L34 (2022).

Acknowledgments: We thank the entire MMS team and instrument principal investigators for providing the data. **Funding:** Q.L. is supported by the National Science Foundation of China (NSFC) 42230201. R.W. is supported by the NSFC 42174187. S.L. is supported by the NSFC 42274196. S.W. is supported by the Project funded by China Postdoctoral Science Foundation (2023M743356) and the Postdoctoral Fellowship Program of CPSF. This work is also supported by the Fundamental Research Funds for the Central Universities and the Strategic Priority Research Program of Chinese Academy of Sciences (grant no. XDB0560000). **Author contributions:** S.W. carried out the spacecraft data analysis and wrote the manuscript. S.L. performed the hybrid simulation and wrote the manuscript. Q.L. and R.W. conceived the idea and oversaw the project. J.R., X.G., and J.G. contributed to the interpretation of the observation and simulation results. All of the authors discussed the results and commented on the paper. **Competing interests:** The authors declare that they have no competing interests. **Data and materials availability:** All data needed to evaluate the conclusions in the paper are present in the paper and/or the Supplementary Materials. The MMS data are publicly available at https://lasp.colorado.edu/mms/sdc/public/about/browse-wrapper/. MMS instruments provide both fast survey mode data and burst mode data. Figures 1, 2, and 5 and fig. S1 used MMS fast survey data, and Fig. 3 and figs. S2 and S3 used MMS burst data. The simulation data used to plot Figs. 4, 5, and 6 and figs. S4, S5, and S6 are archived in https://doi.org/10.6084/m9.figshare.26103565.

Submitted 3 February 2024
Accepted 10 July 2024
Published 14 August 2024
10.1126/sciadv.ado4639